A ZnS/CaZnOS Heterojunction for Efficient Mechanical-to-Optical Energy Conversion by Conduction Band Offset

Dengfeng Peng,[1#] Yue Jiang,[1#] Bolong Huang,[2]* Yangyang Du,[3] Jianxiong Zhao,[3] Xin Zhang,[3] Ronghua Ma,[1] Sergii Golovynskyi,[1] Bing Chen[3] and Feng Wang[3]**

Prof. D. Peng, Y. Jiang, R. Ma, C. Wang, S. Mao, D. Peng, S. Golovynskyi,

College of Physics and Optoelectronic Engineering, Shenzhen University, Shenzhen 518060, China

E-mail: pengdengfeng@szu.edu.cn; #equal contribution

Prof. B. Huang,

Department of Applied Biology and Chemical Technology, The Hong Kong Polytechnic University, Hung Hum, Kowloon, Hong Kong SAR, China

E-mail: bhuang@polyu.edu.hk

Dr. Y. Du, J. Zhao, X. Zhang, Dr. B. Chen, Prof. F. Wang,

Department of Materials Science and Engineering,

City University of Hong Kong, 83 Tat Chee Avenue, Hong Kong SAR, China

mail: fwang24@cityu.edu.hk

Keywords: Mechanoluminescence, ZnS/CaZnOS, Doping, Heterojunction, Light Emission

Abstract: Actively collecting the mechanical energy by efficient conversion to other forms of energy opens the new possibility of energy storage, which is of pivotal significance for supplying potential solutions for the present energy crisis. Such energy conversion has shown promising applications in modern sensors, actuators, and energy harvesting. However, the implementation of such technologies is being hindered because most luminescent materials show weak and non-recoverable emissions under mechanical excitation. Herein, we present a new class of heterojunctioned ZnS/CaZnOS piezophotonic systems, which displays highly reproducible mechanoluminescence with an unprecedented intensity of over 2 times higher than that of widely

used commercial ZnS (the state-of-the-art ML material). Density functional theory calculations reveal that the high-performance ML originates from efficient charge transfer and recombination through valence and conduction bands (VB and CB) offset in the heterojunction interface region. By controlling CaZnOS to ZnS ratios in conjunction with manganese (Mn^{2+}) and lanthanide (Ln^{3+}) doping, tunable ML across the full spectrum is activated by a small mechanical stimulus of 1 N (10 kPa). Our findings demonstrate a novel strategy of constructing efficient ML materials by leveraging interface effects and ultimately promote practical applications for ML.

Introduction

Due to the built-in electric field of the carrier inside the unit, heterojunction is a widely used structure in functional materials for the creation/optimization of desired physical properties. By using the different combinations of materials, various heterojunctions have been constructed and demonstrated for controlling optical[1], electrical[2], mechanical[3] and magnetic characteristics[4]. In particular, semiconductor heterojunctions as the core of light-emitting diodes (LEDs) have played vital roles in electric-driven lighting and display devices. The electric potential of a semiconductor heterojunction has a strong positive effect on charge carrier transport at the interface and can tune/control the behaviors of light emitting[5]. The advances in lighting technology have greatly promoted the development of artificial intelligence, biotechnology and flexible optoelectronics[6]. At present, almost all LEDs are driven by external power supply through wire connecting electrodes. However, the high-efficiency heterojunction material driven by Newton force to achieve the stress light-emitting devices is still limited in the present research. Thus, the exploration of such new type LED without wires and electrodes not only supplies advanced heterojunction systems for ML but also provides a prospective reference for the future multi-approach energy conversion with extended applications.

As a special type of light source, mechanoluminescence (ML) materials are capable of generating photon emissions in response to mechanical stimuli. In comparison with LEDs based on electroluminescence, ML provides sustainable light output by excitation of mechanical energy ubiquitously available in nature. During the past decade, ML materials have attracted widespread interests due to their promising applications in stress sensing, display, artificial skin, bioimaging, anti-counterfeiting, structure fatigue diagnosis, night surveillance and flexible optoelectronics[7-10]. However, the recent developments of high performance ML materials are not as fast as other luminescence systems such as PL/EL, which is attributed to the lack of rational design of ML material systems guided by the in-depth theoretical exploration in the mechanism. ML materials known to date are exclusively homogenous structures, which exhibit the limited optimization space in ML performance. Therefore, further improving the ML performance by exploiting heterostructures remains a challenge for present research [11-12].

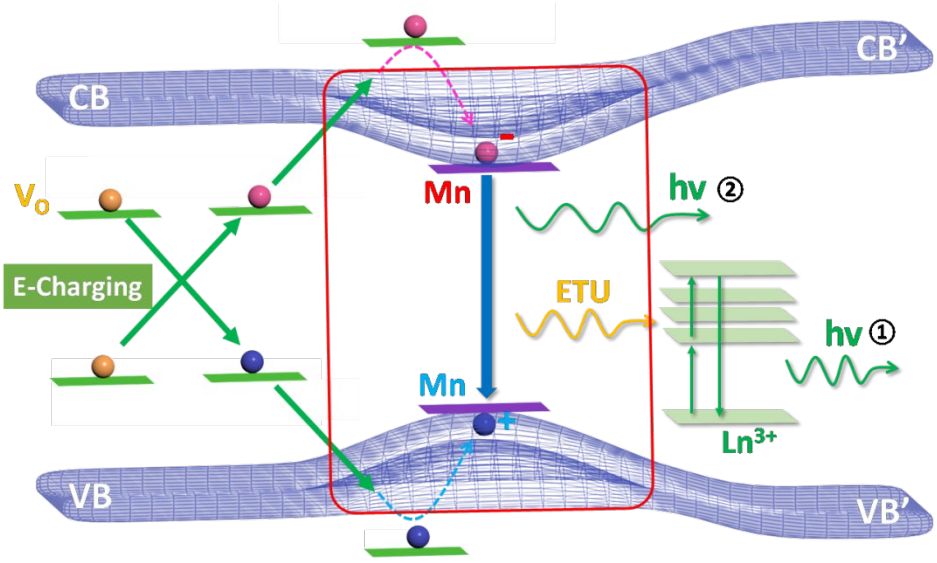

Fig. 1 Scheme of proposed mechanism for mechanical-to-optical energy conversion in the piezophotonic semiconductor heterojunction: the electronic transition in the ML process is facilitated by band offsets at the heterojunction interface region (Indicated by the red frame). VB = valence band; CB = conduction band; E-Charging = electric-field induced charge-separation, ETU = energy transfer upconversion; Ln^{3+} = trivalent lanthanide ion; Orange balls = neutral defect centers; Red balls = electrons; Blue balls = holes.

In this work, we fabricate a class of ZnS/CaZnOS heterostructures, which flexibly tune the efficient and reproducible light generations through the elastic-ML process. Within this process, the photonic excitation is established through strain-induced piezoelectric polarization[11b-e,12-15]. We find that the ZnS/CaZnOS heterojunctions show a competitively intensive and repeatable light-emitting under a gentle fingertip scratching (~1N) without the need for supplementary energy such as ultraviolet light or electrical field/current. The ML intensity is 2.2 times higher than that of commercial ZnS (the state-of-the-art ML material)[8] and 3.5 times higher than that of the well studied CaZnOS[11-15] single counterpart. Our theoretical simulation reveals that band offsets at the heterojunction interface are responsible for the high-performance ML (**Fig. 1**). The interfacial bonding induced band offsets alleviates the electronic excitation barrier from the inter-electronic-level towards conduction band (CB) and promotes the efficiency of electron-hole recombination from the interface electronic levels of activators (*e.g.*; Mn^{2+}). Meanwhile, the released energy of recombination also enables photon emission of tunable colors from lanthanide (Ln^{3+}) dopant levels through energy transfer.

Results and discussions

We choose ZnS and CaZnOS as the host materials because of their known ML properties by doping of Mn^{2+} or lanthanide ions. In addition, they display close compositional and structural similarity (**Fig. 2a**). Hexagonal-phase ZnS and CaZnOS belong to the same space group of P63mc, which form the basis for the construction of high-quality heterojunctions. The ZnS/CaZnOS heterostructures in this work were prepared by a decomposition-combination reaction between $CaCO_3$ and ZnS in an Ar atmosphere at 1100 °C for 4 hr (Supplementary Information). Mn^{2+} ions (1 mol%) were selected as a model dopant to substitute for Zn^{2+} in both

the ZnS and CaZnOS phase. We prepared a series of samples comprising different mass ratios of CaZnOS and ZnS phases by controlling the ratio of $CaCO_3$ and ZnS in the starting materials (**Fig. S1**).

Fig. 2b shows the X-ray powder diffraction (XRD) pattern of a representative sample, which was prepared at a $CaCO_3$ to ZnS ratio of 2:5. All the diffraction peaks are exclusively well assigned to either hexagonal phase ZnS (JCPDS #36-1450) or hexagonal phase CaZnOS (JCPDS #01-076-3819), indicating the formation of ZnS/CaZnOS hybrids. Compositional analysis of the sample by X-ray photoelectron spectroscopy (XPS) and energy-dispersive X-ray spectroscopy (EDS) verifies the presence of the doped elemental Mn (**Fig. S2**). Elemental mapping further reveals the separated segregation of Zn and Ca in different regions within one single particle (**Fig. 2c**), supporting that the final product is indeed composed of ZnS/CaZnOS heterostructure rather than a simple mixture of ZnS and CaZnOS.

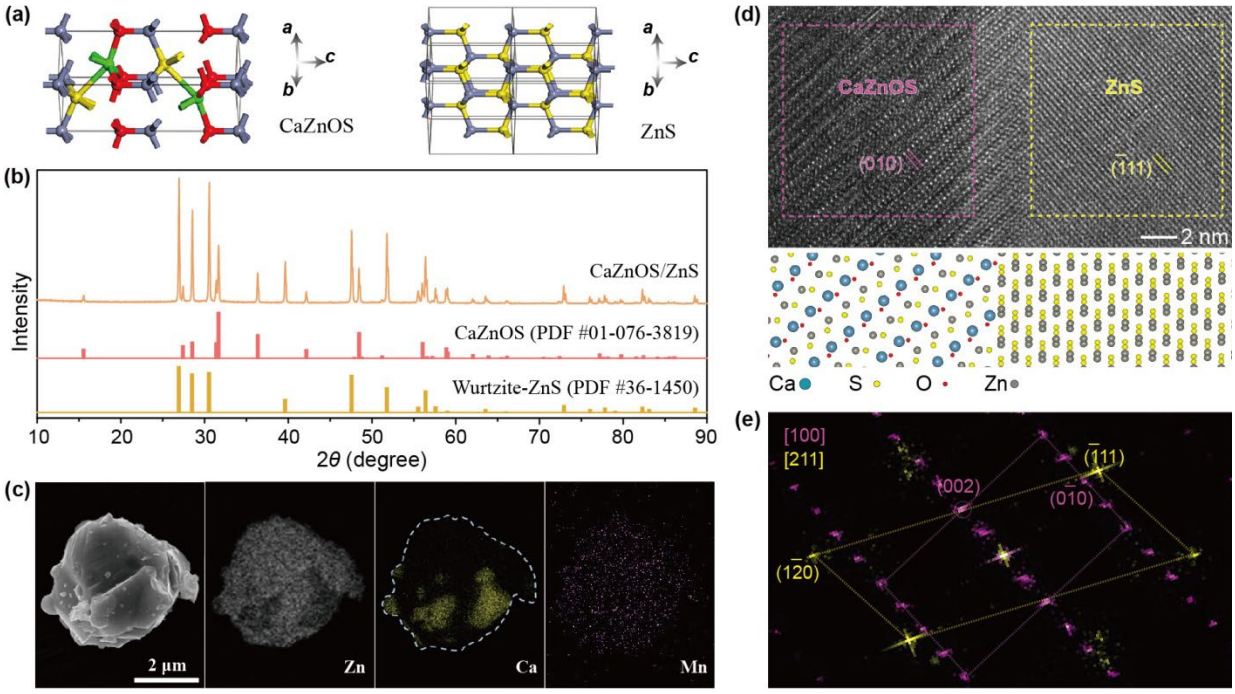

Fig. 2 Crystal structure and chemical compositions of ZnS/CaZnOS heterostructures. (a) Schematic presentation of CaZnOS and hexagonal-phase ZnS structures, respectively. (b) X-ray powder diffraction patterns of ZnS/CaZnOS obtained by annealing ZnS and $CaCO_3$ at molar ratio of 3:2 for 4h at 1100 °C. (c) SEM image and corresponding element maps of a representative ZnS/CaZnOS particle. (d) High-resolution TEM image of a heterojunction in a ZnS/CaZnOS particle. The bottom shows schematic of the crystal structure viewed along the [100] direction of the CaZnOS domain and [211] direction of the ZnS domain. (e) Joint diffractogram obtained by overlapping the FFT patterns of the CaZnOS and ZnS domains (indicated by the magenta and yellow boxes, respectively) in the crystal shown in (d).

Notably, Mn element was detected in all parts of the particles (**Fig. 2c**), indicating the incorporation of Mn into both ZnS and CaZnOS phases. The sample was also characterized by high-resolution transmission electron microscopy (TEM) to confirm the formation of heterojunctions. TEM sample was prepared using the focused ion beam technique (**Fig. S3**). The high-resolution TEM image of a selected region in the particle clearly shows the lattices of both CaZnOS and ZnS phases (**Fig. 2d**). The lattice fringes were continuous across the interface, demonstrating the crystalline nature of the heterojunction with the high quality of epitaxy formation. The fast Fourier transform (FFT) of the high-resolution TEM image (**Fig. 2e**) validates that the crystals on two sides of the interface were CaZnOS and ZnS, respectively.

More importantly, due to the stable formation of heterojunctions with high symmetry of both crystals, we also notice the heterojunctions of different crystallographic orientations (**Fig. S4**).

We next investigate photoluminescence (PL) properties of the ZnS/CaZnOS heterostructure under ultraviolet excitation at 290 nm. PL spectrum of the sample comprised a broad emission

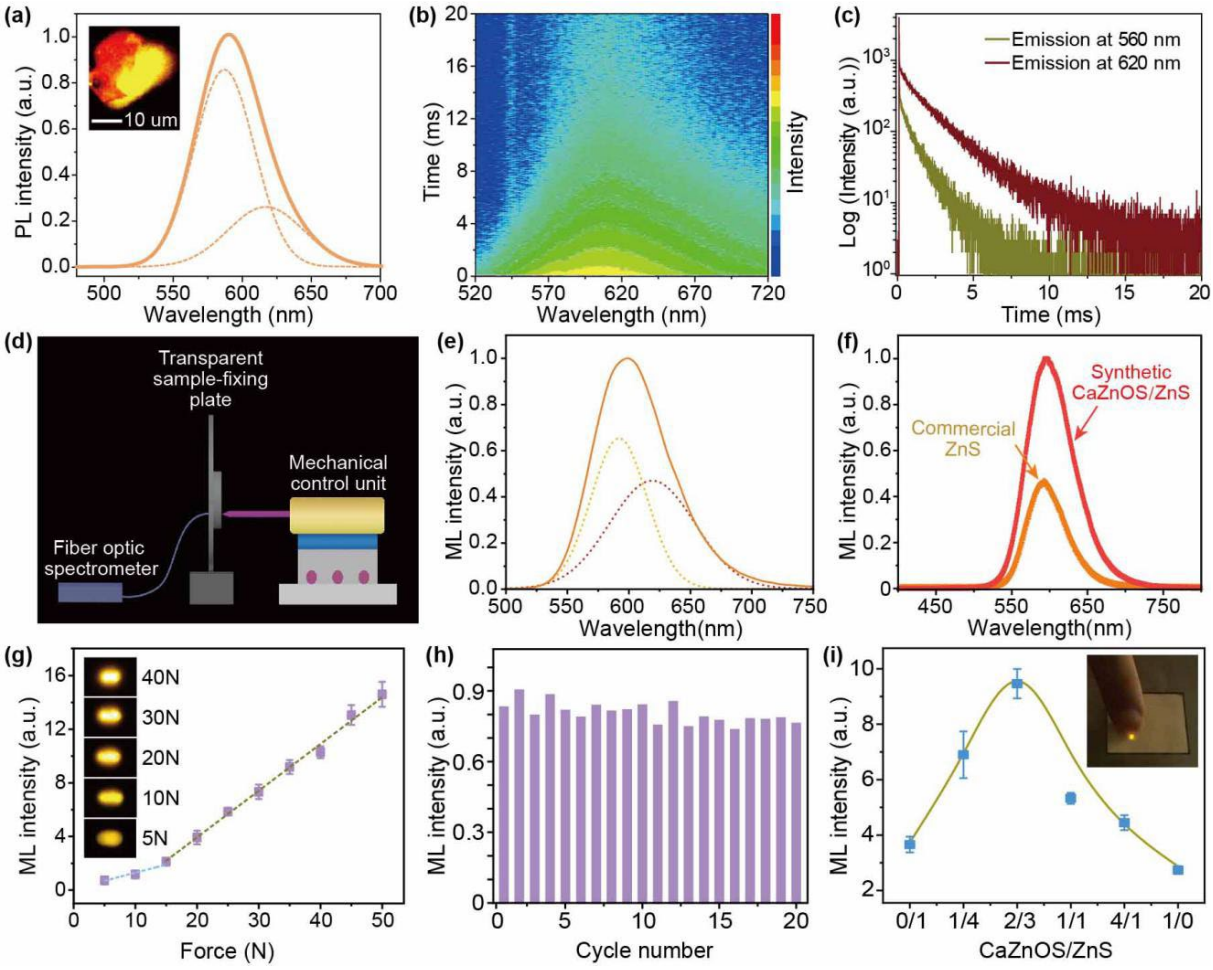

Fig. 3 (a) PL spectrum of the ZnS/CaZnOS heterostructure by UV excitation at 290 nm. Peak analysis shows two components located at 592 and 618 nm ascribing to ZnS:Mn and CaZnOS:Mn, respectively. Inset: optical micrograph of a typical particle. (b) Time-resolved emission spectrum of the sample. (c) Time decay curves of the emissions at 560 and 620 nm, respectively. (d) Schematic of a home-made instrument for ML measurements. A mechanical control unit comprising a linear motor and a pressure gage was used to provide quantitative mechanical excitation to the system. (e) ML spectrum of the ZnS/CaZnOS heterostructures. (f) A comparison of ML intensity between synthetic ZnS/CaZnOS:Mn heterostructures and commercial ZnS:Mn. (g) Integral ML intensity versus applied force for the sample. Inset: ML photograph of the sample sealed in PET film under afferent magnitudes of forces (5-40N). (h) Repeatability of composite films under continuous mechanical excitation at 10N. (i) Integrated intensity over 500~750 nm from ZnS/CaZnOS heterostructures under mechanical excitation at 35N as a function of CaZnOS to ZnS molar ratios. Error bars represent the standard deviations from three repeated measurements. Inset: photograph of the sample with the optimal composition under mechanical excitation with a finger.

peak (**Fig. 3a**), which is resolved into two components centered at 592 and 618 nm corresponding to $^4T_1$ (^4G) → $^6A_1$ (^6S) transition of Mn^{2+} in the ZnS and CaZnOS phases, respectively. Optical micrograph of a typical particle in the inset of **Fig. 3a** shows close correspondence to **Fig. 2c**, which confirms distinct optical emissions from the two phases merged in a single particle. The time decay studies revealed a long excited-state lifetime for Mn^{2+} in both phases (**Fig. 3b** and **3c**) together with a high quantum efficiency of 20% support the high crystalline quality of the heterostructure. The relatively long lifetime of Mn^{2+} in the CaZnOS phase is attributed to the layered host crystal structure. The intrinsic puckered hexagonal layered ZnS and CaO polymorphs units exhibit large spatial separation, resulting in suppression of Mn^{2+}-Mn^{2+} inter-dopant interactions. Based on an efficient radiative process in such heterostructure, we then proceeded to investigate ML properties of the crystals. We found that the as-synthesized samples were very sensitive to stress. We observed bright light emission during the collection of the samples by swaying the corundum boat (**Video S1**) and the package of the sample in a low-density polyethylene (LDPE) plastic bag (**Video S2**). To quantify the ML process, the crystals were enclosed into two pieces of polyethylene terephthalate (PET) films and have been examined using a home-made ML spectrometer (**Fig. 3d** and **Fig. S5**). The observed ML spectrum of the sample (**Fig. 3e**) shows close resemblance to the PL spectrum, suggesting that Mn^{2+} dopants in both ZnS and CaZnOS phases simultaneously contributed to the ML process. It is worth mentioning that the recorded ML intensity is 2.2 times higher than that of commercial ZnS:Mn, the state-of-the-art ML material (**Fig. 3f**). Owing to the protection of the heterojunction materials, the response to the mechanical stimulus has been well preserved, which displayed a linear dependence of emission intensity on the applied force, supporting the previous experimental works[14] (**Fig. 3g**). The samples also showed highly reproducible ML.

Repeatability test of a composite film demonstrated large preservation of ML intensity with continuous dynamic pressure in a dozen days. **Fig. 3h** and **Video S3** show the cycle-dependence intensity of the sample of the initial 20 cycles to confirm the ML repeatability. By contrast, appreciable decay of ML intensity was detected for the single-phase counterpart (**Fig. S6**)[14].

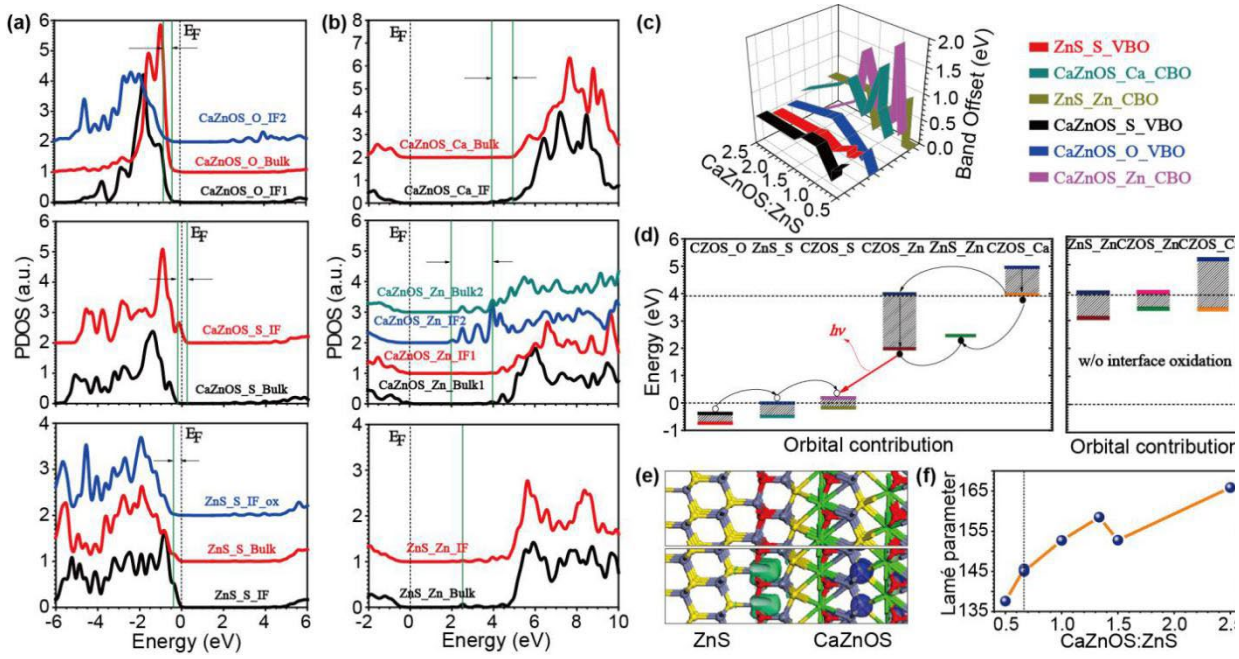

Fig. 4 (a) Projected partial density of states (PDOSs) for O-2p band offsets from the CaZnOS layer, S-3p band offsets from the CaZnOS layer, and S-3p band offsets from ZnS layer, respectively. (d) PDOSs for Ca-3d band offsets from the CaZnOS layer, Zn-3d band offsets from CaZnOS layer, and Zn-3d band offsets from ZnS layer, respectively. (c) Summarized band offsets for both anions and cations with various thickness ratios between CaZnOS and ZnS layers. (d) Band alignments for band offset with and without interface oxidation state. CZOS stands for CaZnOS. (e) Interface atomic structural configuration (top panel) and real spatial contour plots for both HOMO (blue isosurface) and LUMO (green isosurface) localized near the interface region (bottom panel). (f) Variation of Lamé parameters as a function of thickness ratio between CaZnOS and ZnS layers.

Based on energy band theory, the high-performance ML is ascribed to efficient interface charge transfer and recombination through valence and conduction bands (VB and CB) offsets. The interface (IF) of heterojunction is a significant region for the electron-hole spatial separation, which is also the key to determine the photon energy (i.e. wavelength) given by the electron-hole

recombination. Therefore, the VB and CB offsets near the IF region are the pivotal origination for illustrating the origins of high-performance luminescence.

The p-orbitals of anions from both CaZnOS and ZnS layers consist of the valence band accommodating free delocalized holes, while these p-orbitals experience different shifting trends relative to the Fermi level (E_F). The O-2p orbitals from the CaZnOS layer downshift towards deeper levels below the E_F, which ranges from E_V-0.38 eV to E_V-0.74 eV (E_V=0 for E_F). The deep range of O-2p band indicates that the O-2p orbital plays an important role in charge-transfer between cationic and O-sites (**Fig. 4a, top panel**). The S-3p orbitals from CaZnOS layer shift upwards close to the E_F, where the band tail state stays from E_V+0.22 eV to E_V-0.18 eV. The contrasting behavior arises because the S-3p orbital lines up higher position than the O-2p and also covers a wider range, which leads to deeper O-2p orbital levels by strong p-p orbital Coulomb repulsive suppression (**Fig. 4a, middle panel**). The S-3p orbitals from ZnS layer have also been suppressed by the S-3p orbital from CaZnOS layer, which stays from E_F to E_V-0.47 eV. The downshift of S-3p band from ZnS layer indicates the p-p Coulomb inter-orbital repulsion across the interface effecting in a long-range order (**Fig. 4a, bottom panel**). The CB offsets induced by different cationic d-orbital alignments turn to be more evident, which directly determines the intrinsic electronic trapping levels for charge-recombination. The Ca-3d orbital in CaZnOS downshifts from E_V+4.98 eV to E_V+3.96 eV, which is from bulk to the interface region (**Fig. 4b, top panel**). The Zn-3d orbital from CaZnOS offsets vastly from E_V+3.99 eV to E_V+1.98 eV, which is attributed to the O-2p orbital coupling induced strong interfacial oxidation state (**Fig. 4b, middle panel**). However, Zn-3d orbital level from ZnS layer is almost pinned near the CB edge at E_V+2.46 eV (**Fig. 4b, bottom panel**). We further summarized the behaviors of VB and CB offsets from different anions and cations. With the interfacial oxidation state

promoted, the VB offsets are nearly stabilized within a minor shuttle range, while the CB offsets turn out to drastically vary with different layer thickness ratios between CaZnOS and ZnS (**Fig. 4c**). Here we demonstrated that, the CB offsets are strongly correlated with the IF oxidation states given by the O-2p band offset near the IF region, which exhibits a substantial contrast (**Fig. 4d**). This not only lowers down the electronic excitation and transition barrier from VB to CB or inter-electronic-level *via* CB, but also promotes the efficiency of electron-hole recombination for the ML.

As we show from the structural configuration, both IF and deep bulk regions of the ZnS/CaZnOS system possess ordinary bond length without obvious lattice distortion. The IF region consists of polymorphs of -[Zn-O-Zn-S]- as a binding junction (**Fig. 4e, top panel**). The active bonding and anti-bonding orbital near the E_F illustrate the HOMO localizes at the S-sites near the IF from the CaZnOS layer, while the LUMO has been evidently constrained at the Zn-sites at the IF region binding with O-sites (**Fig. 4e, bottom panel**). This indicates an efficient spatial electron-hole separation near the IF region. Due to the spatial truncation and coupling, the intrinsic interfacial-strain (IIS) is also a focus, which produces the driving force on the electronic activities. Accordingly, we computed the Lamé parameters to reflect the correlation within homogenous, isotropic and continuum medium. With increasing CaZnOS layer thickness, the IIS-effect enhances (**Fig. 4f**). Correspondingly, we recall the same ratio variation trend that, the VB offsets turn to be weakened while the CB offsets maintain at an obvious level (**Fig. 4c**). Therefore, the heterojunction at the IF region with anomalous oxidation state induces an intrinsic band offset behavior, which significantly determines the highly efficient ML.

Our further experiments demonstrated that the Ca^{2+} site in the heterostructures accommodates lanthanide dopants for flexible optical tuning. We successfully co-doped a series of lanthanide

ions (e.g.; Pr^{3+}, Ho^{3+}, Tb^{3+}, Dy^{3+}, Eu^{3+}, Sm^{3+}, Yb^{3+}, and Tm^{3+}) together with Mn^{2+} into the ZnS/CaZnOS heterostructures. These samples show emission peaks of both Mn^{2+} and relevant lanthanide ions, with intensities comparable to the Mn^{2+}-doped counterpart (**Fig. 5a** and **Figs. S9-10**). Due to rich energy levels introduced by Er^{3+} ions, we also achieved photon upconversion emission in Mn^{2+}/Er^{3+} co-doped ZnS/CaZnOS heterostructures, in addition to a full-spectrum ML (**Fig. 5b** and **Video S5**). The tunable dual emission provides precise manipulation of the ML color (**Fig. 5c**). The photonic properties available in these heterostructures offer great opportunities for applications in battery-free display, encrypted anti-counterfeiting, e-signature (**Fig. S11**) as well as adaptive optoelectronics and mechanical energy harvesting devices.

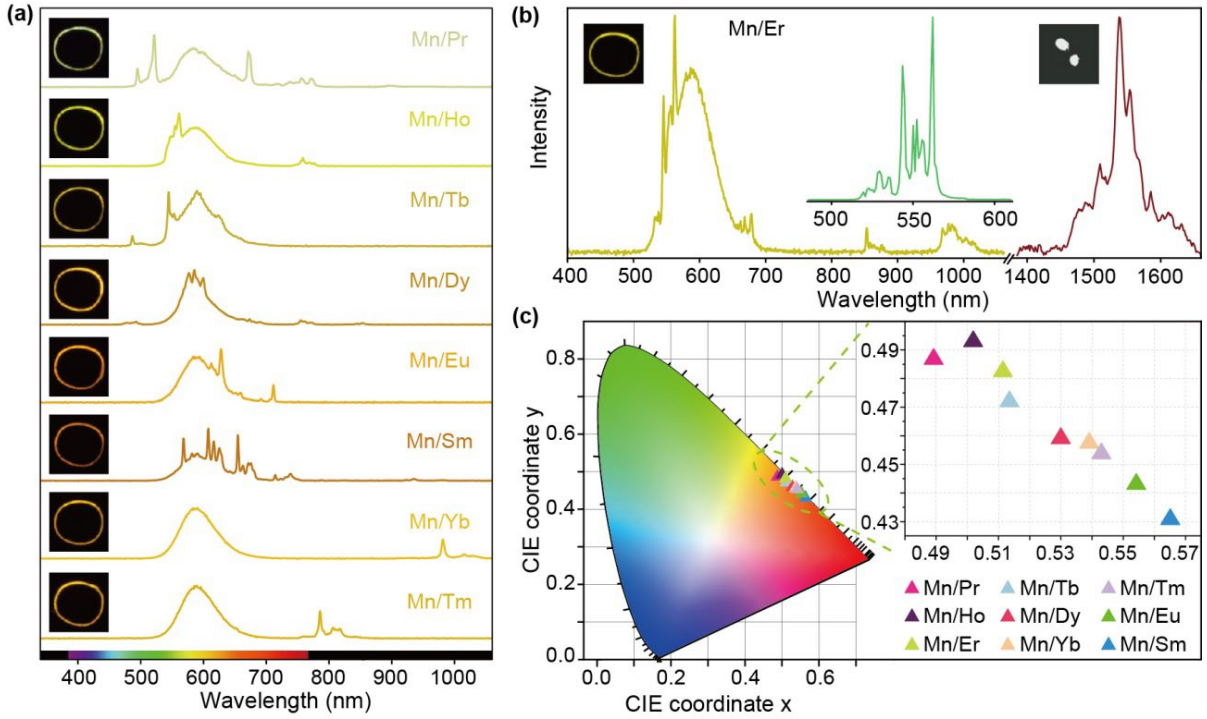

Fig. 5 (a) ML spectra and corresponding photographs of Mn^{2+}/Ln^{3+} (Ln= Pr, Ho, Er, Tb, Dy, Eu, Sm, Yb, and Tm) co-doped ZnS/CaZnOS heterostructures. (b) Full-spectrum ML and near-infrared to visible upconversion (inset) in Mn^{2+}/Er^{3+} co-doped ZnS/CaZnOS heterosructures. (c) Commission International de l'Eclairage (CIE) chromaticity coordinates of the co-doped samples showing precise tuning of the ML color.

Conclusions

In conclusion, we have developed a new and versatile heterostructural engineering approach to construct the ZnS/CaZnOS systems, which demonstrates a remarkable ML performance in both intensity and reproducibility. Detailed characterization confirmed the formation of the heterojunction with well preservation of both crystals. We show that anomalous bonding states in the heterojunction interface region induce substantial band offsets, which lower down the barrier for electronic excitation and transitions involved in the ML process. By constructing a ZnS/CaZnOS heterostructure along with Mn^{2+} and lanthanide doping, we demonstrate bright and tunable ML by gentle scratching with the fingertip (~1 N) without any other supplementary energy such as external UV excitation or electrical field/current driving. Compared to the commercial ZnS systems, the integrated intensity of ML emission has been doubled, which also reaches threefold higher performance than the CaZnOS single counterpart. This novel heterojunction system displays the much-improved ML intensity as well as the reproducibility, which lays a good foundation for the future development of diverse energy conversion devices such as Newton Force driven LEDs. Thus, our work has supplied a novel direction for further optimization of the large numbers of available ML hosts, which represents the untapped potential of heterostructured ML materials for broad optical applications.

Experimental Section

Detailed experimental procedures are reported in the Supporting Information.

Supporting Information

Supporting Information is available from the Wiley Online Library or from the author.

Acknowledgements

This work was supported by the Natural Science Foundation of China (Nos. 61875136, 21771156 and 21773200), Shenzhen Fundamental Research Project (No. 201708183000260),

Shenzhen Peacock Plan (20171010874C), and Scientific Research Foundation as Phase II construction of high level University for the Youth Scholars of Shenzhen University (No. 000002110223). B. Huang is grateful to the Research Grants Council of Hong Kong for an Early Career Scheme (ECS) fund (PolyU 253026/16P). F. Wang acknowledges the Research Grants Council of Hong Kong (CityU 11204717, Project Code: 9042485) and City University of Hong Kong (Project 9667171).

Received: ((will be filled in by the editorial staff))
Revised: ((will be filled in by the editorial staff))
Published online: ((will be filled in by the editorial staff))

References

[1] a) Y. Yan, X. Fang, L. Zhang, Y. Bando, U. K. Gautam, B. Dierre, T. Sekiguchi, D. Golberg, *Nano Lett.*, **2008**, *8*, 2794, b) Y. Zhang G. Y. Gao, H. W. Chan, J. Y. Dai, Y. Wang, J. H. Hao, *Adv. Mater.*, **2012**, *24*,1729, c)X. Y. Li, M. X. Chen, R. M. Yu, T. P. Zhang, D. S. Song, R. R. Liang, Q. L. Zhang, S. B. Cheng, L. Dong, A. L. Pan, Z. L. Wang, J. Zhu, C. F. Pan, *Adv. Mater.* **2015**, *27*, 4447, d) F. Xue, L. B. Chen, J. Chen, J. B. Liu, L. F. Wang, M. X. Chen, Y. K. Pang, X. N.Yang, G. Y. Gao, J. Y. Zhai, Z. L. Wang, *Adv. Mater.*, **2016**, *28*, 3391, e) Y. Zhai, X. Yang, F. Wang, Z. Li, G. Ding, Z. Qiu, Y. Wang, Y. Zhou, S. T. Han, *Adv. Mater.*, **2018**, *30*, 1803563.

[2] a) M. Y. Lu, J. H. Song, M. P. Lu, C. Y. Lee, L. J. Chen, Z. L. Wang, *ACS Nano*, **2009**, *3*, 357, b) W. Wu, X. Wen, Z. L.Wang, *Science*, **2015**, *340*, 952, b) F. Withers, O. D. Pozo-Zamudio, A. Mishchenko, A. Rooney, A. Gholinia, K. Watanabe, T. Taniguchi, S. Haigh, A. Geim and A. Tartakovskii, *Nat. Mater.*, **2015**, *14*, 301, c) X. F. Wang, R. M. Yu, C. Y. Jiang, W. G. Hu, W. Z. Wu, Y. Ding, W. B. Peng, S. Li, Z. L. Wang, *Adv. Mater*. **2016**, *28*, 7234, d) K. Ding, J. Wang, Y. Zhou, H. Tian, L. Lu, R. Mazzarello, C. Jia, W. Zhang, F. Rao and E. Ma, *Science*, **2019**, *366*, 210.

[3] J. W. Jiang and H. S. Park, *Appl. Phys. Lett.*, **2014**, *105*, 033108.

[4] M. Mogi, M. Kawamura, R. Yoshimi, A. Tsukazaki, Y. Kozuka, N. Shirakawa, K. Takahashi, M. Kawasaki and Y. Tokura, *Nat. Mater.*, **2017**, *16*, 516.

[5] a) Z. L. Wang, *Nano Today*, **2010**, *5*, 540,b) Z. L. Wang, *J. Phys. Chem. Lett.* **2010**, *1*, 1388,c) Z. L. Wang, *Adv. Mater.*, **2012**, *24*, 4632, d) Y. Liu, S. M. Niu, Q. Yang, B. D. B. Klein, Y. S.Zhou, Z. L. Wang, *Adv. Mater.* **2014**, *26*, 7209, e) C. Pan, M. Chen, R. Yu, Q. Yang, Y. Hu, Y. Zhang, Z. L. Wang, *Adv. Mater.*, **2016**, *28*, 1535,f) W. Wu, Z. L. Wang,

Nat. Rev. Mater., 2016, 1, 16031, g) C. Pan, J. Zhai, Z. L. Wang, *Chem. Rev.*, **2019**, *119*, 9303..

[6] a) S. Pimputkar, J. S. Speck, S. P. DenBaars and S. Nakamura, *Nat. photonics*, **2009**, *3*, 180, b) C. Wang, D. Hwang, Z. Yu, K. Takei, J. Park, T. Chen, B. Ma, A. Javey, *Nat. Mater.*, **2013**, *12*, 899. c) X. Dai, Z. Zhang, Y. Jin, Y. Niu, H. Cao, X. Liang, L. Chen, J. Wang, X. Peng, *Nature*, **2014**, *515*, 96, d) J. Lee, P. W. Bisso, R. L. Srinivas, J. J. Kim, A. J. Swiston, P. S. Doyle, *Nat. Mater.*, **2014**, *13*, 524,e) C. Larson, B. Peele, S. Li, S. Robinson, M. Totaro, L. Beccai, B. Mazzolai, R. Shepherd, *Science*, **2016**, *351*, 1071, f) D. H. Lien, S. Z. Uddin, M. Yeh, M. Amani, H. Kim, J. W. Ager, E. Yablonovitch, A. Javey, *Science*, **2019**, *364*, 468.

[7] a) P. Jha, B. P. Chandra, *Luminescence*, **2014**, *29*, 977, b) D. Peng, B. Chen, F. Wang, *Chem Plus Chem*, **2015**, *80*, 1209, c) A. Feng, P. F. Smet, *Materials*, **2018**, *11*, 484, d) J. Xie, Z. Li, Chem, **2018**, *4*, 943, e) J. G. Bünzli, K. L. Wong, *Journal of Rare Earths*, **2018**, *36*, 1, f) J. Hao and C. N. Xu, *MRS Bull.*, **2018**, *43*, 965, g) H. Zhang, Y. Wei, X. Huang, W. Huang, *J. Lumin.*, **2019**, *207*, 137, h) X. Wang, D. Peng, B. Huang, C. Pan, Z. L. Wang, *Nano Energy*, **2019**, *55*, 389, j) J. C. Zhang, X. Wang, G. Marriott, C. N. Xu, *Prog. Mater. Sci.*, **2019**, *103*,678.

[8] a) C. N. Xu,T. Watanabe, M. Akiyama, *Appl. Phys. Lett*. **1999**, *74*, 1236, b) S. Moon Jeong, S. Song, S. K. Lee, B. Choi, *Appl. Phys. Lett.*, **2013**, *102*, 051110,c) S. M. Jeong, S. Song, S. K. Lee and N. Y. Ha, *Adv. Mater.*, **2013**, *25*, 6194, d) S. M. Jeong, S. Song, K. I. Joo, J. Kim, S. H. Hwang, J. Jeong, H. Kim, *Energy Environ. Sci.*, **2014**, *7*, 3338, e) X. Wang, H. Zhang, R. Yu, L. Dong, D. Peng, A. Zhang, Y. Zhang, H. Liu, C. Pan, Z. L. Wang, *Adv. Mater.*, **2015**, *27*, 2324, f) L. Chen, M. C. Wong, G. Bai, W. Jie and J. Hao, *Nano Energy*, 2015, **14**, 372, g) S. M. Jeong, S. Song and H. Kim, *Nano Energy*, **2016**, *21*, 154, h) H. Fang, X. Wang, Q. Li, D. Peng, Q. Yan, C. Pan, *Adv. Energy Mater.*, **2016**, *6*, 1600829, i) D. K. Patel B. E. Cohen , L. Etgar, S. Magdassi, *Mater. Horiz.*, **2018**, *5*, 708 , j) X. Qian, Z. R. Cai, M. Su, F. Y. Li, W. Fang, Y. D. Li, X. Zhou, Q. Y. Li, X. Q. Feng, W. B. Li, X. T. Hu, X. D.Wang, C. F. Pan, Y. L. Song, *Adv. Mater.* **2018**, *30*, 1800291, k) S. Song, B. Song, C. H. Cho, S. K. Lim, S. M. Jeong, *Materials Today*, **2019**, *in press*, doi.org/10.1016/j.mattod.2019.08.004, l) L. Liu, C. N. Xu, A. Yoshida, D. Tu, N. Ueno and S. Kainuma, *Adv. Mater. Technol.*, **2019**, ***4***, 1800336,

[9] a) D. Tu, C. N. Xu, A. Yoshida, M. Fujihala, J. Hirotsu, X. G. Zheng, *Adv. Mater*., **2017**, *29*, 1606914, b) J. C. Zhang, C. Pan,Y. F. Zhu, L. Z. Zhao, H. W. He, X. F. Liu, *Adv. Mater*. **2018**, *30*, 1804644, c) C. Wu, S. S. Zeng, Z. F. Wang, F. Wang, H. Zhou J. C. Zhang, Z. P. Ci, L. Y. Sun, *Adv. Funct. Mate*r. **2018**, *28*, 1803168, d) T. Jiang, Y. F. Zhu, J. C. Zhang, J. J. Zhu, M. Zhang, J. R. Qiu, *Adv. Funct. Mater.* **2019**, 1906068,

[10] a) J. C. Zhang, C. N. Xu, S. Kamimura, Y.Terasawa, H. Yamada, X. S. Wang, *Optics Express*, **2013**, *21*, 12976, b) D Tu, CN Xu, Y Fujio, S Kamimura, Y Sakata, N Ueno, *Appl. Phys. Lett.* ,**2014**, *105*, 011908, c) D Tu, CN Xu, Y Fujio, A Yoshida,*Light: Science & Applications*, **2015**, *4*, e356, d) J. C. Zhang, L. Z. Zhao, Y. Z. Long, H. D. Zhang, B. Sun, W. P. Han, X. Yan, X.S. Wang, *Chem. Mater*. **2015**, *27*, 7481

[11] a) X. W. Levision, *Science*, **1904**, *19*, 826, b) G. AlZetta, X. Minnaja, S. Santucci, *Il Nuovo Cimento*, **1962**, *5*, 910, c) V. K. Chandra, B. P. Chandra, P. Jha, *Appl. Phys. Lett.* **2013**, *103*, 161113, d) V. K. Chandra,B. P. Chandra,P. Jha, *Appl. Phys. Lett.* **2013**, *102*, 241105, e) B. P. Chandra, V. K. Chandra, P. Jha, *Appl. Phys. Lett.* **2014**, *104*, 031102

[12] B. Huang, D. Peng and C. Pan, *Phys. Chem. Chem. Phys.*, **2017**, *19*, 1190.

[13] a) H. L. Zhang, D. F. Peng, W. Wang, L. Dong, C. F. Pan, *J. Phys. Chem. C*, **2015**, *119*, 28136, b) D. Tu. D. F. Peng,C. N. Xu, A. Yoshida, *J Ceram. Soc. Jpn*, **2016**, *124*,702, c) W Wang, D Peng, H Zhang, X Yang, C Pan,*Opt. Commun.*, **2017**, *395*, 24.
[14] Y. Du, Y. Jiang, T. Sun, J. Zhao, B. Huang, D. Peng, F. Wang, *Adv. Mater.*, **2019**, *31*, 1807062.
[15] B. Huang, *Phys. Chem. Chem. Phys.*, 2016, **18**, 25946.

Keywords: Mechanoluminescence, ZnS/CaZnOS, Doping, Heterojunctions, Light Emission

Dengfeng Peng,[1#] Yue Jiang,[1#] Bolong Huang,[2]* Yangyang Du,[3] Jianxiong Zhao,[3] Xin Zhang,[3] Ronghua Ma,[1] Sergii Golovynskyi,[1] Bing Chen[3] and Feng Wang[3]**

Title: A ZnS/CaZnOS Heterojunction for Efficient Mechanical-to-Optical Energy Conversion by Conduction Band Offset

ToC figure ((Please choose one size: 55 mm broad × 50 mm high **or** 110 mm broad × 20 mm high. Please do not use any other dimensions))

Supporting Information

A ZnS/CaZnOS Heterojunction for Efficient Mechanical-to-Optical Energy Conversion by Conduction Band Offset

Dengfeng Peng,[1#] Yue Jiang,[1#] Bolong Huang,[2]* Yangyang Du,[3] Jianxiong Zhao,[3] Xin Zhang,[3] Ronghua Ma,[1] Sergii Golovynskyi,[1] Bing Chen[3] and Feng Wang[3]**

[1]College of Physics and Optoelectronic Engineering, Shenzhen University, Shenzhen 518060, China

[2]Department of Applied Biology and Chemical Technology, The Hong Kong Polytechnic University, Hung Hum, Kowloon, Hong Kong SAR, China

[3]Department of Materials Science and Engineering, City University of Hong Kong, 83 Tat Chee Avenue, Hong Kong SAR, China

Experimental Sections

Reagents. $CaCO_3$ (99.99%, Alfa Aesar), ZnS (>97%, Sinopharm Group Co. Ltd.), $RE(NO_3)_3 \cdot XH_2O$ (

RE = Pr^{3+}, Ho^{3+}, Tb^{3+}, Dy^{3+}, Eu^{3+}, Sm^{3+}, Yb^{3+}, Er^{3+} and Tm^{3+}) (99.99%, Sinopharm Group Co. Ltd.) and $MnCO_3$ (>98%, Alfa Aesar) were all purchased and used as received.

Sample preparation. For the Mn-doped ZnS sample, ZnS and $MnCO_3$ were homogeneously mixed and ground in agate mortar followed by calcination at 1050~1150°C for 2~8 hours under Ar atmosphere (purity, 99.99%). The sintered product was naturally cooled to room temperature in the furnace and grounded again into powders for subsequent characterizations and use. For the Mn-doped CaZnOS samples, $CaCO_3$ was a popular precursor material for the Ca and O elements. Stoichiometric amounts of $CaCO_3$ into ZnS, $MnCO_3$ and $LiF/LiNbO_3$ (1mol %) were used as starting materials.[1] For the Mn- and lanthanide-doped CaZnOS samples, $CaCO_3$ and $RE(NO_3)_3 \cdot xH_2O$ were first mixed and ground for 10 minutes and then mixed with ZnS and $MnCO_3$ for 30 minutes to obtain a uniform mixture. To evaluate the ML properties of the doped CaZnOS phosphors, as-synthesized ML crystals were mixed with polydimethylsiloxane (PDMS) and sealed uniformly between two square polyethylene glycol terephthalate (PET) sheets following a home-made photographic-plasticization process.

Reagents reaction:

The chemical reactions in preparation of doped ZnS and CaZnOS, ZnS/CaZnOS

① ZnS:Mn: $ZnS\ (Blend) + xMnCO_3 \rightarrow ZnS{:}Mn\ (Wurtzite) + CO_2\uparrow$

② CaZnOS:Mn: $CaCO_3 \rightarrow CaO + CO_2\uparrow$

$$CaO + ZnS + xMnCO_3 \rightarrow CaZnOS{:}Mn + CO_2\uparrow$$

③ ZnS/CaZnOS:Mn: $CaCO_3 \rightarrow CaO + CO_2\uparrow$

$$CaO + ZnS + xMnCO_3 \rightarrow ZnS/CaZnOS{:}Mn$$

④ Mn- and lanthanide-doped ZnS/CaZnOS:

$$CaCO_3 \rightarrow CaO + CO_2\uparrow$$
$$RE(NO_3)_3 \cdot XH_2O \rightarrow RE_2O_3 + H_2O\uparrow + NO_2\uparrow$$
$$RE_2O_3 + CaO + ZnS + xMnCO_3 \rightarrow ZnS/CaZnOS{:}Mn/RE$$

Physical measurements. X-ray diffraction (XRD) patterns were recorded by a Bruker D2 phase X-ray diffraction analyzer to examine the crystal structure of the as-prepared ML particles. X-ray photoelectron spectrum was acquired on Scanning Auger XPS Model 5802 (PHI, USA). SEM

images of as-prepared samples were obtained from a 3 Hitachi SU 8020 scanning electron microscope. Energy dispersive X-ray element maps were obtained on a HOBIRA EMAX X-ray detector. The FIB sectioning of craters was carried out on an FIB microscope (FEI Scios) using the incident beam energy of 30 kV Ga+. Morphology study and element distribution were conducted by SEM (Zeiss SUPRA-55) and TEM (JEM-3200FA, JEOL). Optial micrograph was recorded on a Nikon Eclipse Ti-U inverted microscope equipped with a Nikon Digital Sight DS-Fi2 camera (Nikon, Japan) at 20x optical magnification. Photoluminescence (PL) spectra were obtained by a Hitachi F-4600 spectrophotometer equipped with a R928 photomultiplier (PMT) detector. The ML emission spectra were recorded by a home-built measuring apparatus. A ball-point stick was fixed on a linear motor to apply periodic sliding forces on the thin-film sample by moving the pen tip forth and back. An Ocean Optics QE65pro fiber optic spectrometer in the wavelength range of 200-1000 nm was used to collect the ML signals from the sample that was supported by an acrylic sheet. Customized Ocean Optics fiber spectrometers operating in the spectral range of 300-1100 nm and 900nm-1700nm respectively was used to measure the ML spectra of Er^{3+}, Tm^{3+}, Nd^{3+} and Yb^{3+} doped samples. The luminance of the samples is recorded by a spectroradiometer. The magnitude of forces applied to the sample were adjusted through a three-dimensional stage and monitored by a force sensor. The pressure distribution image was acquired by long-exposure photography using a digital camera. Unless otherwise stated, all measurements were carried out at room temperature.

Theoretical calculations. We built various ZnS/CaZnOS interface models using the host CaZnOS lattice with P63mc space group, which is the same as the symmetry of wurtzite ZnO. For the interface construction, we have cleaved the (010) surface of CaZnOS and (111) surface of ZnS to investigate the formation of the interface and the related electronic environment to different local sites. The layer thickness ratio of ZnS/CaZnOS has been varied from 0.5 to 2.0 for the mechanical properties investigations.

The related theoretical calculations have been performed by PBE+U calculations with CASTEP code.[2] Regarding the valence states, the (3s, 3p, 3d, 4s) states for Ca, (3d, 4s, 4p) for Zn, (3s, 3p) for S, and (2s, 2p) for O have been chosen, respectively. We used OPIUM code in the Kleinman-Bylander form norm-conserving pseudopotential[3] with non-linear partial core correction[4] to

minimize the systematic error due to the atomic core-valence electron densities overlap. Further, the RRKJ method was chosen to optimize the basis sets and ionic minimization of pseudopotentials.[5] The kinetic cutoff energy of 850 eV, which expands the valence electrons states in a plane-wave basis set. To guarantee the electronic minimization and convergence, the ensemble DFT (EDFT) method of Marzari et al[6] was used for iteratively minimizing the system Kohn-Sham equation. The reciprocal space integration was performed by k-point sampling with grids of 2 × 2 × 1 for ZnS/CaZnOS interfacial electronic structures calculations in periodic supercell accordingly. The calculation converges the total energy to be lower than 5.0×10-7eV per atom. The Hellmann-Feynman force on each atom was converged to lower than 0.01eV/Å. The geometry optimization used the Broyden-Fletcher-Goldfarb-Shannon (BFGS) algorithm through all bulk and defect supercell calculations. With our self-consistently determination process,[7-13] the on-site Hubbard U parameters for 3d of Ca and Zn are 2.50 eV, 13.45 eV, 2.87 eV for the 3p of S, and 3.44 eV for the 2p of the O, respectively.

References

1 Y. Du, Y. Jiang, T. Sun, J. Zhao, B. Huang, D. Peng and F. Wang, *Adv. Mater.*, 2019, **31**, 1807062.

2 S. J. Clark, M. D. Segall, C. J. Pickard, P. J. Hasnip, M. I. Probert, K. Refson and M. C. Payne, *Z. Krist.-Cryst. Mater.*, 2005, **220**, 567-570.

3 L. Kleinman and D. Bylander, *Phys. Rev. Lett.*, 1982, **48**, 1425.

4 S. G. Louie, S. Froyen and M. L. Cohen, *Phys. Rev. B*, 1982, **26**, 1738.

5 A. M. Rappe, K. M. Rabe, E. Kaxiras and J. Joannopoulos, *Phys. Rev. B*, 1990, **41**, 1227.

6 N. Marzari, D. Vanderbilt and M. C. Payne, *Phys. Rev. Lett.*, 1997, **79**, 1337.

7 B. Huang, *J. Comput. Chem.*, 2016, **37**, 825-835.

8 B. Huang, *Solid State Commun.*, 2016, **230**, 49-53.

9 B. Huang, *Solid State Commun.*, 2016, **237**, 34-37.

10 B. Huang, *Phys. Chem. Chem. Phys.*, 2016, **18**, 13564-13582.

11 B. Huang, *Inorg. Chem.*, 2015, **54**, 11423-11440.

12 B. Huang, R. Gillen and J. Robertson, *J. Phys. Chem. C*, 2014, **118**, 24248-24256.

13 B. Huang, *Philos. Mag.*, 2014, **94**, 3052-3071.

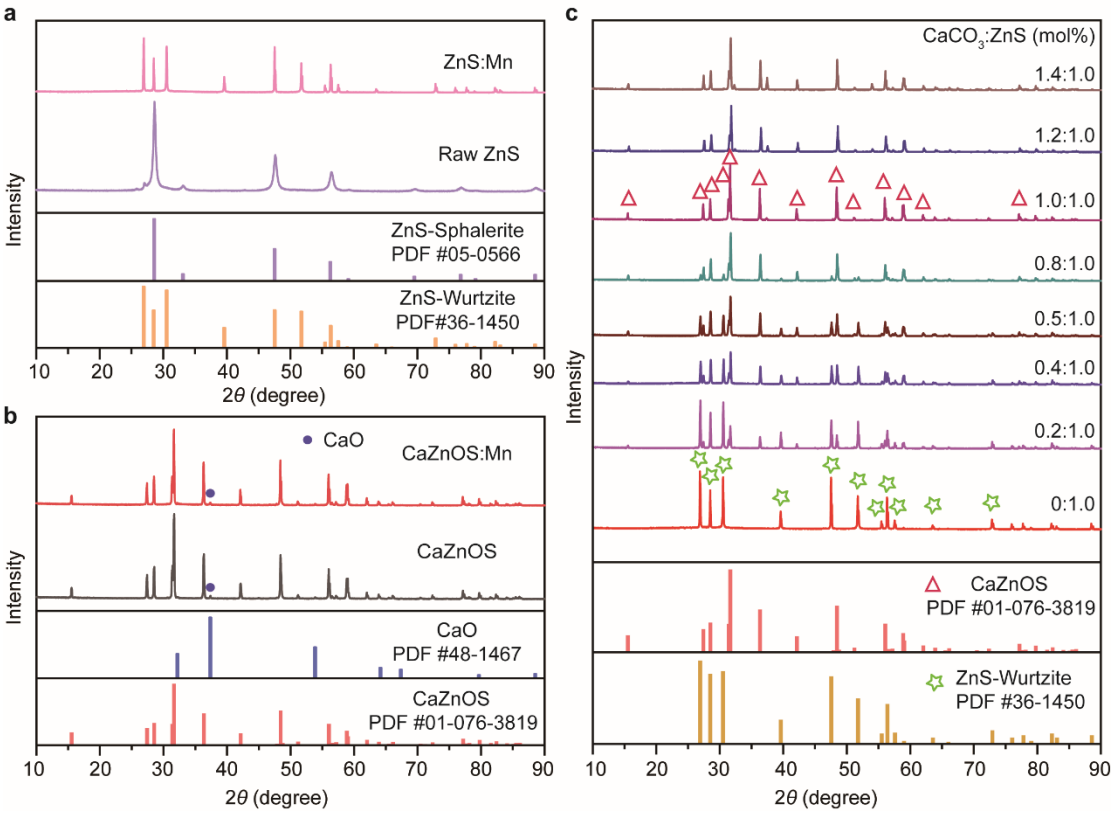

Figure S1. (a) XRD of the Mn doped wurtzite ZnS (hexagonal structures) from raw sphalerite ZnS (cubic structures) annealed for 4h at 1100 ℃ under Argon atmosphere, indicating a phase transformation of the ZnS. (b) XRD spectra of the CaZnOS prepared by annealing ZnS and $CaCO_3$ with/without $MnCO_3$ for 4h at 1100℃ under Argon atmosphere. (c) XRD spectra of ZnS/CaZnOS prepared at varying molar ratios of ZnS and $CaCO_3$ in the starting materials. Excess $CaCO_3$ ($CaCO_3$: ZnS > 1) was found to result in single phase CaZnOS and minor CaO impurity. No impurity phases of Mn compounds were detected, suggesting that Mn^{2+} ions were incorporated into the host lattice.

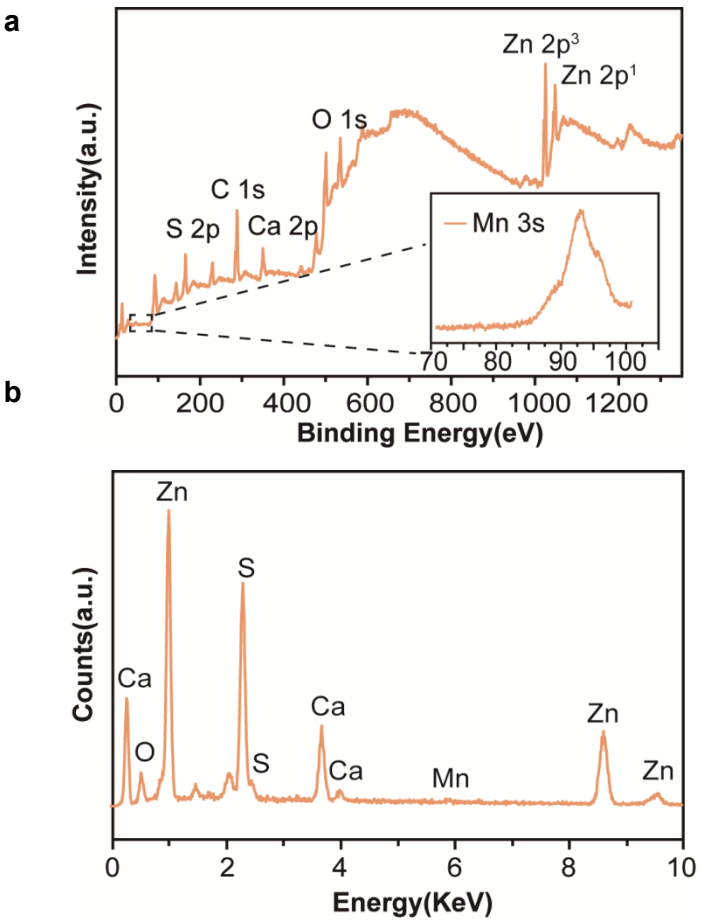

Figure S2 (a) XPS and (b) EDS spectra taken from the Mn-doped ZnS/CaZnOS heterostructure, revealing the presence of constituent elements.

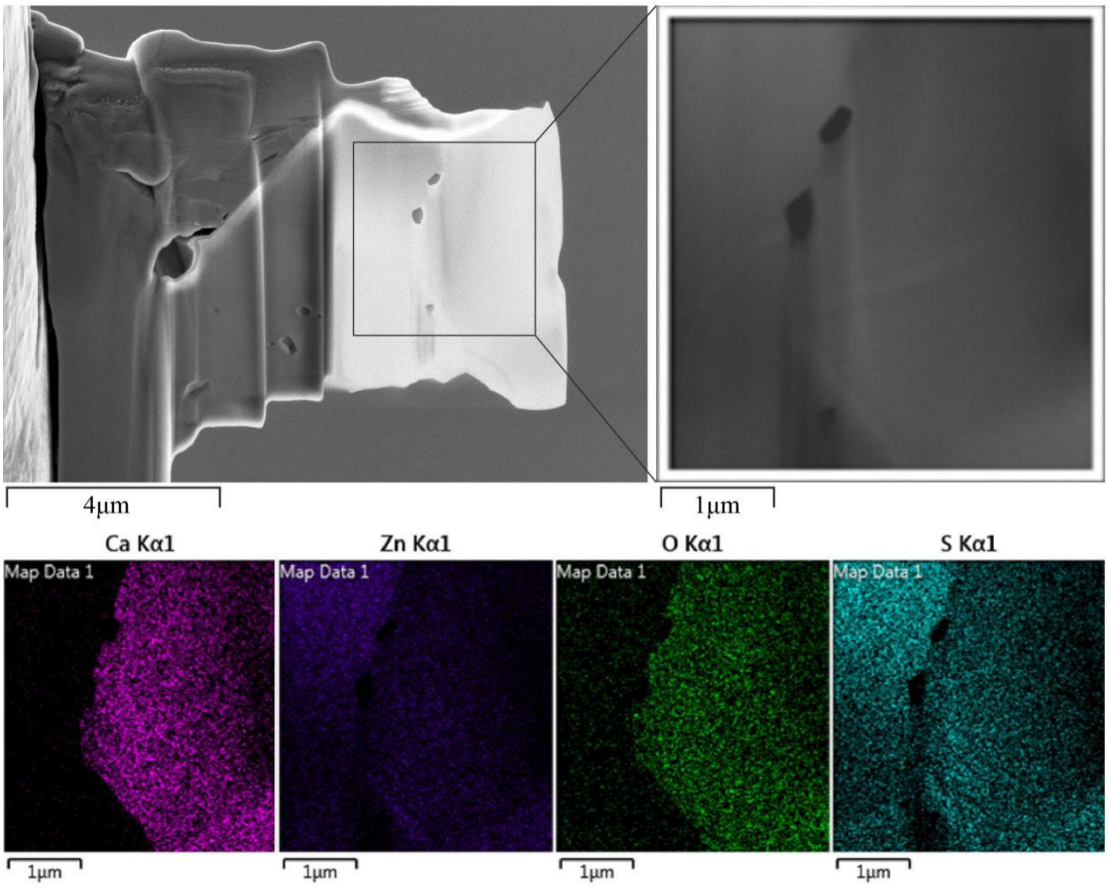

Figure S3 SEM image and corresponding EDS element mapping for a ZnS/CaZnOS heterostructure after treatment by focused ion beam (FIB) (FEI, Scios) technique, showing the boundary between the ZnS and CaZnOS phases.

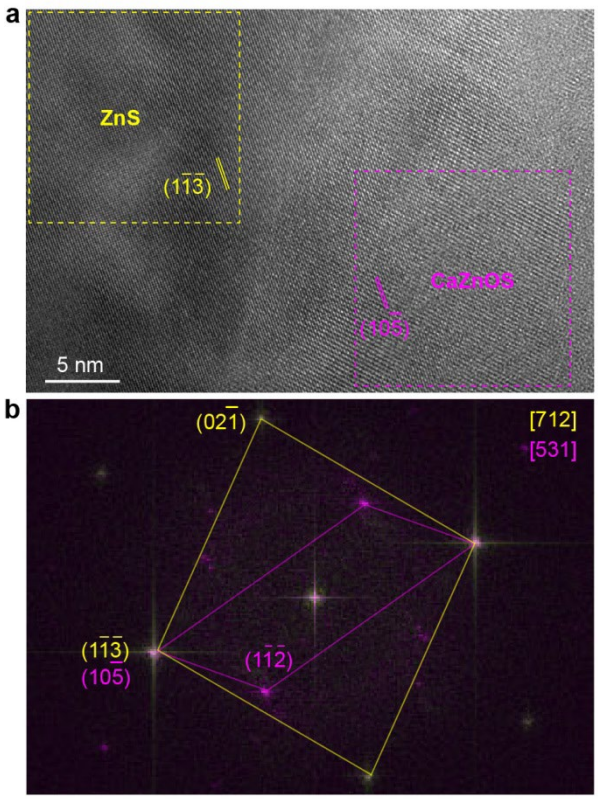

Figure S4 (a) High-resolution TEM image of a heterojunction in a ZnS/CaZnOS particle. (b) Joint diffractogram obtained by overlapping the FFT patterns of the CaZnOS and ZnS domains (indicated by the magenta and yellow boxes, respectively) in the crystal shown in (a)

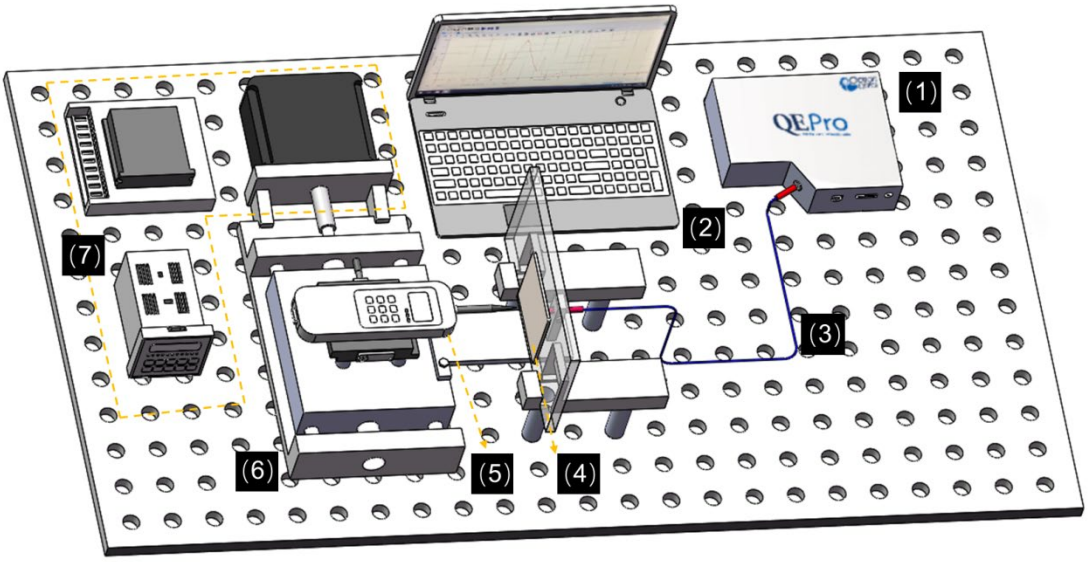

Figure S5 Schematic of the home-made instrument for mechanoluminescence measurements. (1) fiber optic spectrometer (Ocean Optics QE65 pro), (2) PC, (3) optic fiber, (4) transparent sample-fixing plate, (5) pressure gage, (6) 3-D displacement platform, (7) control unit for linear motor.

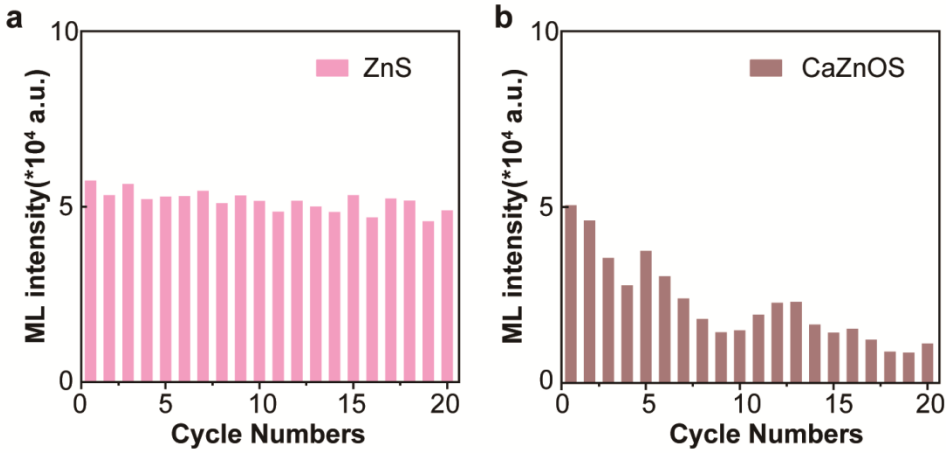

Figure S6 Repeatability test of composite film samples. Integrated mechanoluminescence intensity over 500–850 nm under continuous mechanical action at 10 N for (a) ZnS:Mn and (b) CaZnOS:Mn.

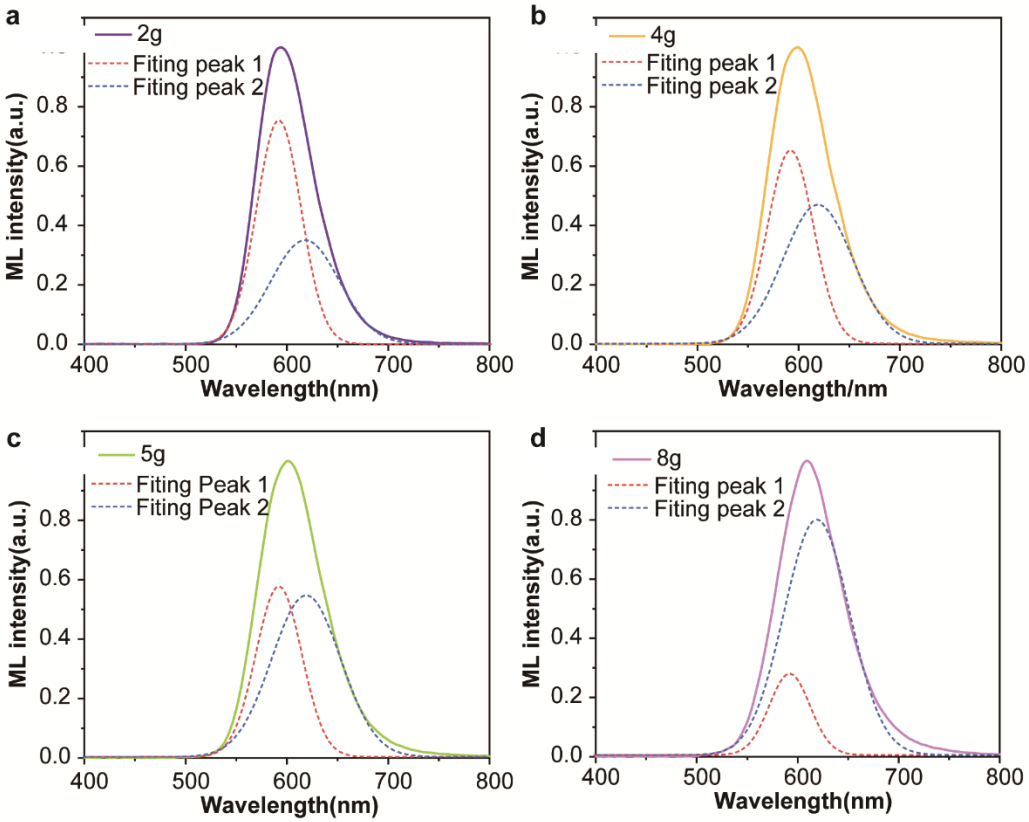

Figure S7 ML spectra and peaks analyses of ZnS/CaZnOS prepared at $CaCO_3$ to ZnS ratios of (a) 0:2.0, (b) 0.4:1.0, (c) 0.5:1.0 and (d) 0.8:1.0 in the starting materials. As the amount $CaCO_3$ increased, the CaZnOS became the dominating phase in the final product, leading to a red-shift of the emission spectra.

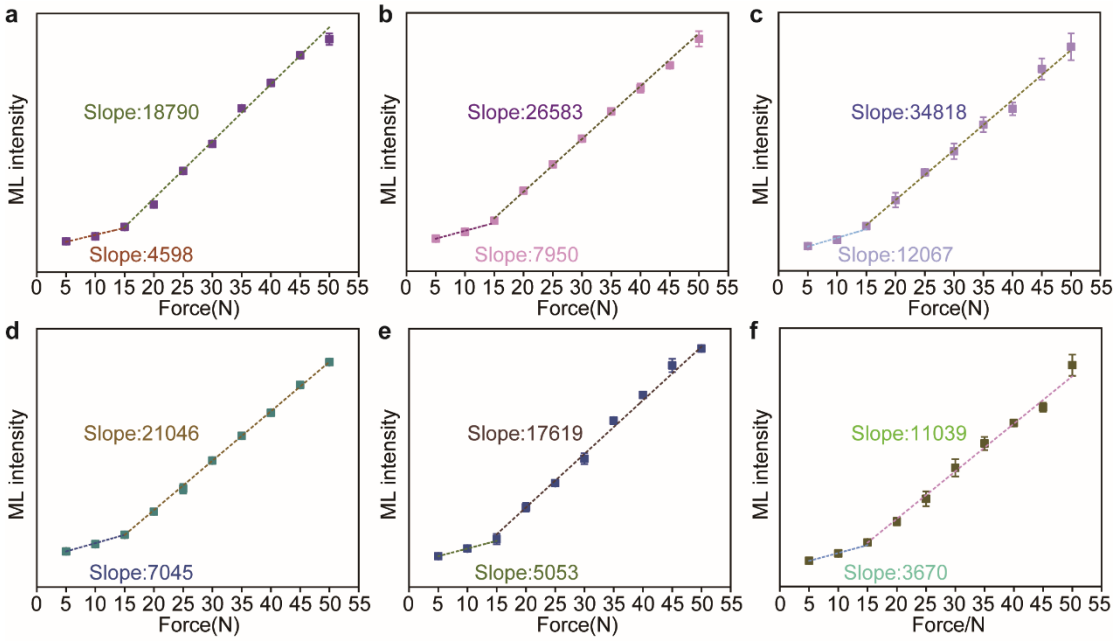

$CaCO_3$:ZnS(mol%)	0:1.0	0.2:1.0	0.4:1.0	0.5:1.0	0.8:1.0	1.0:1.0
Slope1	4598	7950	12067	7045	5053	3670
Slope2	18790	26583	34818	21046	17619	11039

Figure S8 Integral ML intensity versus applied force for ZnS/CaZnOS prepared at $CaCO_3$ to ZnS ratios of (a) 0:1.0, (b) 0.2:1.0, (c) 0.4:1.0, (d) 0.5:1.0, (e) 0.8:1.0 and (f) 1.0:1.0 in the starting materials. According to the fitted slopes, the sample prepared with ZnS:CaZnOS ratio of 3:2 displayed the highest sensitive to mechanical stimuli.

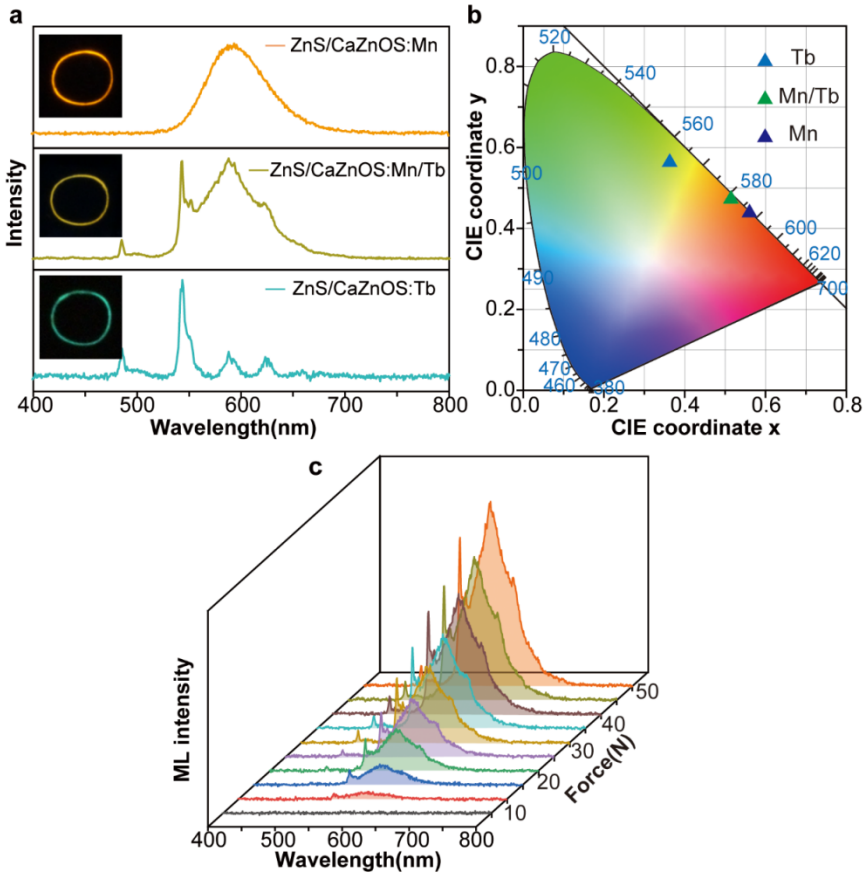

Figure S9 (a) Comparison of mechanoluminescence for ZnS/CaZnOS:Mn, ZnS/CaZnOS:Mn/Tb and ZnS/CaZnOS: Tb. (b) The corresponding Commission International de l'Eclairage (CIE) chromaticity coordinates for the samples. (c) ML spectra recorded by mechanical excitation of different strengths.

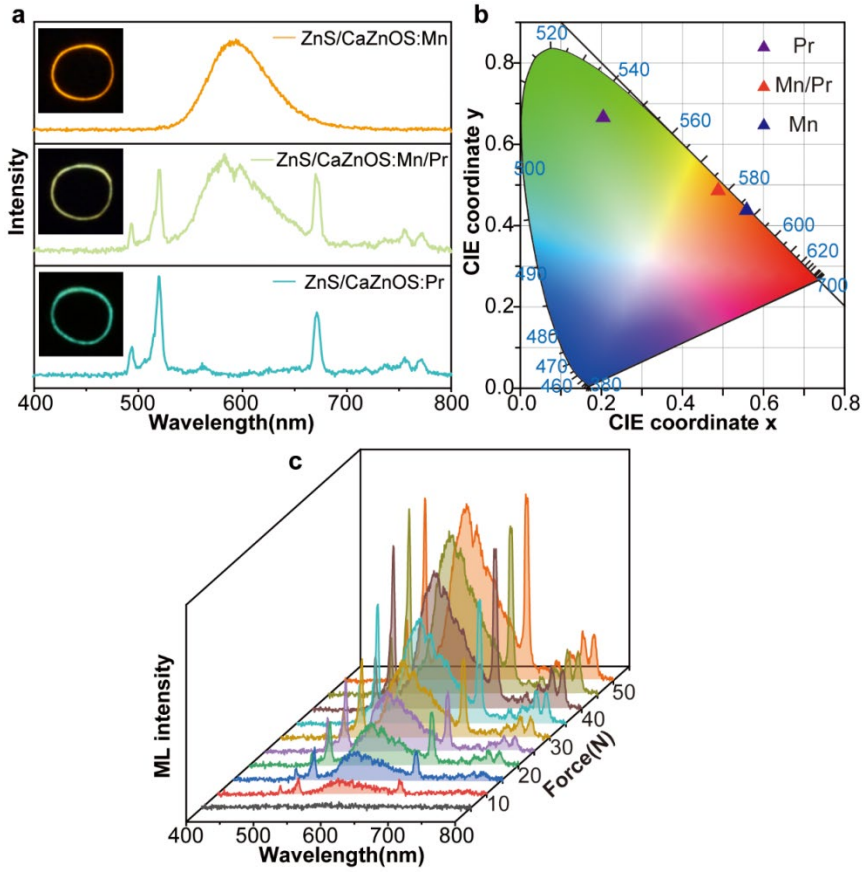

Figure S10 (a) Comparison of mechanoluminescence for ZnS/CaZnOS:Mn, ZnS/CaZnOS:Mn/Pr and ZnS/CaZnOS:Pr. (b) The corresponding Commission International de l'Eclairage (CIE) chromaticity coordinates for the samples. (c) ML spectra recorded by mechanical excitation of different strengths.

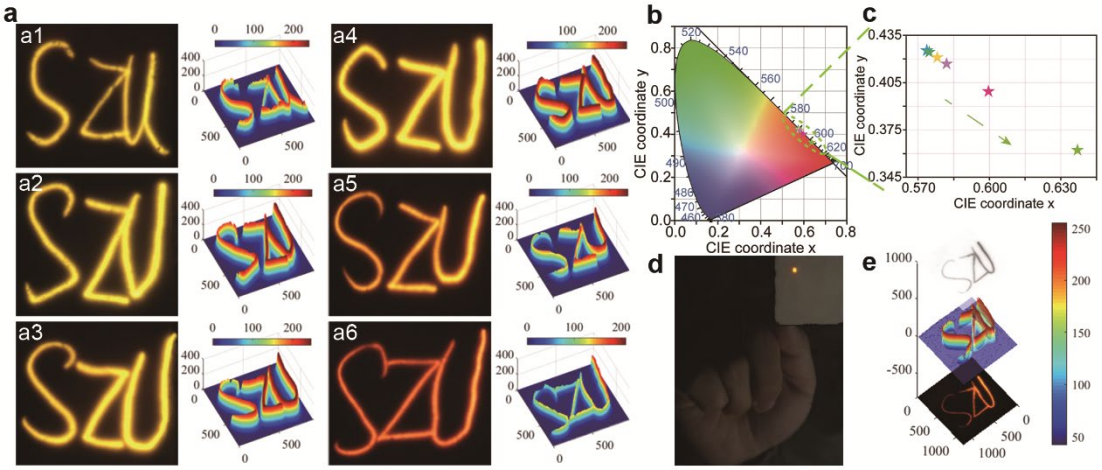

Figure S11 Photograph of the ML samples by the fingertip scratching through long-time exposure. (a1-a6) correspond to samples with CaZnOS/ZnS ratios of 0:1, 1:4, 2:3, 1:1, 4:1 and 1:0, respectively. (b, c) Commission International de l'Eclairage (CIE) chromaticity coordinates of the different samples showing in figure (a). (d, e) Acquisition of handwriting habit using the ML thin-film. Pressure information can be extracted from the ML intensity profile for E-signature applications.